A Portable, Four-wavelength, Single-cell Photoacoustic Spectrometer for Ambient Aerosol Absorption

Al Fischer and Geoffrey D. Smith
University of Georgia, Athens, GA 30602 USA

Abstract. Aerosols directly affect Earth's climate by scattering and absorbing solar radiation. Although they are ubiquitous in Earth's atmosphere, direct, *in-situ*, wavelength-resolved measurements of aerosol optical properties remain challenging. As a result, the so-called aerosol direct effects are one of the largest uncertainties in predictions of Earth's future climate, and new instrumentation is needed to provide measurements of the absorption of sunlight by atmospheric particles. We have developed a portable, four-wavelength, single-cell photoacoustic spectrometer for simultaneous measurement of aerosol absorption at 406, 532, 662, and 785 nm, with an additional extinction measurement at 662 nm via a built-in cavity ringdown spectrometer. The instrument, dubbed MultiPAS-IV, is compact, robust, has low power requirements, and utilizes a multipass optical arrangement to achieve typical detection limits of 0.6 – 0.7 Mm^{-1} for absorption (2σ, 2-minute average). Tests with nigrosin aerosols show agreement with Mie theory calculations to within 2%, and comparison with a 7-wavelength aethalometer shows good correlation for ambient (Athens, Georgia) aerosols. We demonstrate the utility of the broad spectral coverage and sensitivity of the MultiPAS-IV for calculating the absorption Ångström exponent of black carbon (AAE_{BC}, median value of 0.70) in ambient aerosols and use this value to derive the brown carbon contributions to absorption at 406 nm (43%) and 532 nm (13%) and its wavelength dependence (AAE_{BrC} = 6.3).

1. Introduction

Atmospheric aerosols directly affect Earth's climate by scattering and absorbing solar radiation, thereby altering the radiative balance of the Earth. Uncertainties on aerosol effects are among the largest for making predictions of Earth's future climate, and aerosol optical properties have thus become an area of intense research in recent years (Stocker et al. 2014). Absorbing aerosols consist primarily of carbonaceous aerosols and mineral dust. Two species compose light absorbing carbonaceous aerosols: black carbon (BC), which results from combustion of fossil fuels, biofuels, and biomass and absorbs light relatively evenly throughout the UV-visible spectrum, (Bond et al. 2013) and brown carbon (BrC), which results from incomplete combustion, smoldering biomass, and secondary and biogenic sources and absorbs primarily at ultraviolet and blue wavelengths (Kirchstetter et al. 2004; Andreae and Gelencser 2006).

Aerosol absorption has historically been a difficult quantity to measure, and (Moosmüller et al. 2009) provide an extensive review of measurement techniques. Many methods involve collecting aerosols on a filter, extracting the collected particulate matter, and measuring the UV-visible spectrum of the soluble fraction with a spectrophotometer. These methods are still widely employed with great utility but suffer from well-known artifacts associated with filter collection and extraction, most notably that the optical properties are measured in solution and not of suspended aerosol. Other filter-based methods involve collecting aerosols on a filter and measuring changes in the transmission through the filter in real-time and are employed by instruments such as the aethalometer and the particle soot/absorption photometer (PSAP). These methods are well known to suffer from artifacts related to the filter, including filter-loading and multiple scattering effects that can lead to a higher perceived absorption compared to *in-situ* measurements (Weingartner et al. 2003; Lack et al. 2008; Drinovec et al. 2015). The multiangle absorption photometer (MAAP) corrects for multiple scattering by measuring direct and diffuse backscattering by the filter (Petzold and Schönlinner 2004), though it still can suffer from filter loading effects.

The so-called “subtraction method" does not rely on a filter but instead calculates the absorption from the difference of extinction and scattering by suspended particles (Singh et al. 2014). However, at large single scattering albedo (SSA) values when extinction is dominated by scattering, typical of many ambient aerosols, even a modest 3% error in the SSA can translate to a large error (60%) in absorption calculated from the difference (Onasch et al. 2015). Typically, the least error-prone methods for measuring aerosol absorption are photothermal methods in which light absorbed by particles creates a thermal/pressure wave, which is detected with a microphone (photoacoustic spectroscopy) or an interferometer (optical homodyne interferometry) (Lin and Campillo 1985; Moosmüller et al. 1997; Sedlacek and Lee 2007). Because these methods measure absorption by suspended particles directly, they avoid filter-based artifacts and potentially large uncertainties possible with the subtraction method. Of the photothermal methods, photoacoustic spectroscopy (PAS) has been most widely applied, likely due to the relative simplicity of the equipment, the feasibility of creating compact, portable instruments, and the availability of commercial instruments. PAS, in rudimentary form, was first described by Alexander Graham Bell but was not widely applied until the mid- to late-twentieth century due to a lack of technology to make the technique viable (Bell 1881; Miklos et al. 2001). In 1977, (Truex and Anderson 1979) made the first reported PAS measurements of aerosol absorption, and since then it has seen increasing application in aerosol science due to its insensitivity to scattering, which makes it well suited for measuring aerosol absorption.

The first portable PAS instruments for measuring aerosol absorption at wavelengths in the visible (532 and 685 nm) (Arnott et al. 1999) and near-IR (802 nm) (Petzold and Niessner 1995) were developed in the 1990s with detection limits reaching < 1 Mm^{-1}. In 2006, Arnott and co-workers reported the first PAS measurements of aerosol absorption aloft (Arnott et al. 2006), while in the same year Lack et al. demonstrated enhanced sensitivity by employing a multi-pass laser (532 nm) alignment with a limit of detection of 0.08 Mm^{-1} (Lack et al. 2006). Arnott and co-workers later combined two lasers (405 and 870 nm) in a single photoacoustic cell providing spectral coverage while simplifying operation by requiring calibration at only one wavelength (Lewis et al. 2008). That instrument evolved into a three-wavelength (405, 532, 781 nm) version commercialized as the PASS-3 (Droplet Measurement Technologies; Boulder, CO). Ajtai et al. expanded spectral coverage by using the fundamental (1064 nm) and three higher-order harmonics (266, 355, 532 nm) of a Nd:YAG laser with four separate cells (Ajtai et al. 2010; 2011). Lack et al. deployed three of their multipass instruments (404, 532, 659 nm) on an aircraft with detection limits of 0.5 – 1.5 Mm^{-1} (Lack et al. 2012), and Cappa and co-workers continue to use similar instruments (405 and 532 nm) to make a variety of laboratory- and field-based measurements (e.g. (Zhang et al. 2016)). Recently, Haisch et al. (Haisch et al. 2012) has used a tunable optical parametric oscillator and Sharma et al. (Sharma et al. 2013) and Radney and Zangmeister (Radney and Zangmeister 2015) have employed supercontinuum lasers to measure aerosol absorption in the laboratory at wavelengths throughout the visible and near-IR regions of the spectrum; these can take on the order of several to tens of minutes to collect a spectrum and are not yet portable. In 2014, our group developed a Hg lamp-based instrument able to measure absorption at eight narrow wavelength bands from 301 nm to 687 nm (Wiegand et al. 2014), though it, like the supercontinuum-based instruments, has a low duty cycle and is not field deployable.

Here, we describe a photoacoustic instrument for measuring aerosol absorption at four wavelengths (406, 532, 662, and 785 nm) contained in a single acoustic resonator, which we call the MultiPAS-IV. The instrument employs a multipass design to increase sensitivity, which is based on the design of Lack et al. (Lack et al. 2006; 2012) but differs in that it is the first such implementation with a single set of mirrors for four wavelengths in a single photoacoustic cell. This design affords us the advantage of a single calibration applicable to all wavelengths, just like other multi-wavelength, single-cell instruments, thus reducing errors in measuring the wavelength dependence of the absorption. In that sense, it is similar to the PASS-3 instrument and the three-wavelength (445, 532, 660 nm) PAS of Linke et al. (Linke et al. 2016); however, we show how the ability to measure at blue, green, red, and near-IR wavelengths allows us to measure the wavelength dependence (i.e. absorption Ångström exponent) of the BC component (AAE_{BC}) and subsequently the contribution by BrC and the AAE_{BrC}, as well. Consequently, it is not necessary to assume particle mixing state or the BC spectral shape (e.g. AAE) as is commonly done. We demonstrate how the small size, weight, and power requirements coupled with the sub-Mm^{-1} detection limits of the instrument make it uniquely capable of making such measurements with ambient aerosols even under relatively clean conditions.

2. Materials and Methods

2.1 Instrument description

The photoacoustic instrument described herein is designed to measure absorption by aerosols at four wavelengths in the visible and near-IR region of the spectrum. It employs four lasers coupled into a single acoustic resonator. The acoustic signals for each wavelength are measured simultaneously, and one of the lasers is split to a cavity ringdown (CRD) spectrometer for calibration of the PAS and as a simultaneous measure of extinction during aerosol sampling. The system is compact, low power (< 400 W), lightweight (34 kilograms), and is mounted in a standard Pelican case (63 cm x 50 cm x 37 cm) for easy transport.

2.1.1 Operating principles

Both PAS and CRD have been thoroughly described elsewhere, including detailed accounts of their applications to aerosols. (Arnott et al. 1999; Miklos et al. 2001; Brown 2003; Lack et al. 2006; Berden and Engeln 2009; Moosmüller et al. 2009), so they will be described only briefly here. In PAS, signal is generated only by absorbed light. When a sample absorbs light modulated at an acoustic frequency (typically 1-2 kHz) it will induce a pressure wave detectable with a microphone. The intensity of the microphone signal is then directly proportional to the absorption by the sample. Typically, the modulation frequency is chosen to match a resonant frequency of the sample cell, thereby achieving resonant amplification.

For CRD, we use a wide-bandwidth (1 nm) diode laser to excite many longitudinal modes of a high-finesse optical cavity consisting of two highly reflective mirrors (R = 99.9985%) (Fuchs et al., 2009). When light couples into the cavity, an intensity build up is observed, and when the laser is quickly switched off the light decays exponentially with a decay constant, τ, on the order of tens of microseconds. This time constant provides a direct measurement of the extinction coefficient, α_{ext}, if the baseline (aerosol-free) ringdown time, τ_0, is known:

$$\alpha_{ext} = \frac{R_l}{c}\left(\frac{1}{\tau} - \frac{1}{\tau_0}\right) \quad (1)$$

Here, R_l is the ratio of the total mirror-to-mirror cavity length to the occupied sample cell length and accounts for purge volumes protecting each of the mirrors, and c is the speed of light.

2.1.2 Acousto-opto-mechanical system

The general opto-mechanical system for the MultiPAS-IV is shown in Figure 1. It employs four diode lasers (Coherent OBIS) that emit at 406, 532, 662, and 780/785 nm with powers of 80 mW (532 nm) and 100 mW (406, 662, 780/785 nm). We note that the when the 785 nm laser was repaired partway through the project, the laser diode was replaced resulting in a shift to a wavelength of 780 nm; thus we list this laser as "780/785 nm." All data presented in this work were collected with the 785 nm laser except for the nigrosin experiments (Figure 4), which employed the 780 nm laser. The beams from each of the four lasers pass through Faraday isolators to minimize back reflections into the lasers and then to a series of dichroic mirrors (Semrock) to make them co-linear. Once combined, the beams are turned with a mirror into a multipass cell consisting of two custom-coated cylindrical mirrors with reflectivity >99% at each of the PAS wavelengths (25.4 mm diameter, f = 50 mm, Eksma/Altos Photonics). The front mirror contains a 2 mm central aperture to allow entry of the laser beams and is held in a rotatable mount to allow alignment of the cylindrical mirrors with respect to each other until a dense multipass pattern is produced (Silver, 2005). Theoretically, as many as 200 passes are possible with such an arrangement (Silver 2005), though in practice we measure the effective power enhancements at each wavelength, which are functions of the window transmission and mirror reflectivity, and are 30x, 40x, 56x, 40x for 406, 532, 662, and 785 nm, respectively.

[Figure 1]

The custom-machined, aluminum PAS sample cell is placed between the multipass mirrors such that the beam pattern is transmitted through the acoustic resonator inside the cell and the custom AR-coated windows (Evaporated Coatings, Inc.) with transmission > 99.5% on either end of the cell. The resonator is 150 mm long and 25 mm in diameter with λ/4 acoustic filters on either end to reduce noise from the windows; its design has been described elsewhere (Lack et al., 2006; Lack et al., 2012). An optoacoustic microphone (Optimic 4110) is placed at the center point of the resonator for transduction of the signal. The resonant frequency of the cell, typically 1400 Hz for nitrogen at room temperature, is determined by monitoring the microphone signal as the modulation frequency of one of the lasers is scanned. The quality factor, Q, of the resonant mode is 30, as determined from the full width at half maximum of the frequency scan (Lack et al. 2006) (see Figure S1 in the Supplemental Information).

The small amount of light passing through the rear multipass mirror is turned and focused onto a photodiode (Thorlabs PDA100A) with a 50 mm focal length concave mirror (Thorlabs CM508-050-E02) for continuous monitoring of effective laser power within the cell. Most of the PAS optics are mounted in a cage system to minimize thermal drift and avoid misalignments. Particle losses through the PAS cell are measured to be < 5% while there are no NO_2 losses within measurement uncertainty.

The CRD operates only at 662 nm. A 90:10 beamsplitter (Thorlabs BSX10) is used in place of a dichroic mirror such that 10% of the 662 nm beam is sent to the CRD cell, which consists of two highly reflective mirrors (R=99.9985%, FiveNine Optics) 25.4 mm in diameter and with a focal length of 0.5 m. The mirrors are held in custom-machined mounts that are in turn held in standard kinematic mirror mounts (Thorlabs KM100). Light exiting the rear of the cavity passes through a bandpass filter and is focused onto an avalanche photodiode (APD, Thorlabs APD410A) for detection. The sample enters and exits the cavity through 1/4" stainless steel tubing connected to the cell at 45 degrees; a purge of 50 standard cubic centimeters (SCCM) of nitrogen (Airgas) is maintained over each mirror using a critical orifice (Lenox Laser) to avoid deposition of particles.

2.1.3 Electronics and data acquisition

For simultaneous acquisition of signal at all four wavelengths, the lasers are digitally modulated near the resonant frequency of the cell with square waves at four separate frequencies generated by a microcontroller (32 bit 180 MHz ARM Cortex-M4/Teensy 3.6, PJRC.com). These frequencies are spaced by 2 Hz to eliminate interference when they are deconvolved. A 24-bit USB sound card (ICUSBAUDIOMH, Startech.com) sampling at 44 kHz digitizes the signal collected by the microphone. A custom LabVIEW program is used to process the signal and perform a fast Fourier transform (FFT) to deconvolute the four laser signals. An identical sound card is used to digitize the photodiode signal, and a FFT is similarly performed to monitor the effective power at each wavelength.

For CRD, the APD signal is sent to an oscilloscope (PicoScope 2000A), which acquires the decays and stores them in an on-board buffer before sending a block of waveforms to LabVIEW. Once in LabVIEW, the decays are co-added and fit to an exponential function using the discrete Fourier transform method (Mazurenka et al. 2005; Everest and Atkinson 2008; Bostrom et al. 2015).

2.2 Calibration

The PAS is calibrated using NO_2 gas (1-5 ppm in N_2) with the CRD measuring the absolute absorbance at 662 nm. A regression of the PAS signal against the CRD absorption gives the PAS cell's calibration coefficient. Because the same laser is used for both the CRD and PAS, any uncertainties in the laser wavelength and/or NO_2 absorption cross-section are irrelevant. An example calibration plot is shown in Figure S2a (Supplemental Information) demonstrating the validity of this approach with close agreement between measurements of NO_2 absorption at 532, 662, and 780 nm. We also note that this approach is similar to the calibration procedure for other PAS instruments, including the PASS-3 in which NO_2 or kerosene soot is used to calibrate the cell at 532 nm and this calibration is used for the other wavelengths (405 and 781 nm). To apply the same calibration coefficient to each channel, though, the relative powers of each of the lasers must be known. Thus, the photodiode behind the PAS is used to measure the effective power in the cell and is calibrated to a thermal power meter (Thorlabs S310C) by removing the PAS cell from the optical setup and measuring the power and photodiode signal of a single pass. The laser power is varied electronically, and the regression slope of the photodiode signal vs. the laser power provides the photodiode calibration factor at each wavelength.

2.3 Ambient sampling

Ambient sampling was conducted from the Chemistry Building on the campus of University of Georgia in Athens, GA (33.948869, -83.374632) during March 2017. Athens may be considered a clean sub-urban site in terms of air quality with few local sources of aerosols during early spring aside from traffic. As such, the aerosols may be considered well-aged, “background" aerosols.

2.3.1 PAS and CRD

For PAS and CRD measurements, air was drawn through a Nafion membrane dryer (Perma-Pure) with a N_2 (Airgas) sheath flow and dried to <10% relative humidity. Aerosols were carried through a short length of 1/4" conductive silicone tubing (TSI, Inc.) to an automated valve (N-Research). The valve was controlled by the LabVIEW program and alternately allowed aerosol-laden air to pass for 24 minutes and then HEPA-filtered air for five minutes. This filtered measurement included contributions from any gas-phase absorbers, such as NO_2, which were then subtracted from the aerosol measurements. In a polluted environment in which the concentrations of such species are large, rapidly changing concentrations over the sampling period could skew aerosol absorption measurements, though we point out that most other PAS instruments are affected by the same issue. An additional minute was used to measure the resonant frequency of the cell by scanning the 406 nm modulation frequency and then to automatically adjust the frequency of all lasers accordingly. Since the resonant frequency of the cell is a function of temperature (2 Hz/ºC), this frequent adjustment accounted for any temperature drift that may have occurred over the previous 30 minutes. Three fans mounted to the case provided exchange of air but otherwise there was no active temperature regulation. After exiting the PAS cell, the sample flowed through a small length of grounded copper tubing to the CRD cell and then to a critical orifice (200 micrometer hole diameter, Lenox Laser) and diaphragm pump (KNF Neuberger, Inc.) that sets the total flow rate (330 SCCM). Flows larger than 400 SCCM were found to increase acoustic noise substantially, presumably from turbulent flow. Data were saved by the LabVIEW program.

2.3.2 Aethalometer

An AE33 7-wavelength, dual-spot aethalometer with Teflon-coated glass fiber filter tape was used for aethalometer measurements (Magee Scientific). Air was drawn through a silica-gel diffusion dryer (RH < 10%) and delivered to the aethalometer via the 1/4" conductive tubing provided by the manufacturer. The aethalometer’s built in pump was used to provide flow at the factory-default flow rate, and all other default setting were likewise used for the aethalometer. Specifically, it was set to report data every 60 seconds with a 5-minute rolling average. Data were logged directly to the aethalometer and retrieved after sampling for post-processing. A multiple-scattering correction factor or 1.57 (Drinovec et al. 2015) was applied internally by the aethalometer.

2.3.3 SMPS

Particle size distributions were collected every five minutes by using a scanning mobility particle sizing spectrometer (SMPS; TSI 3080 electrostatic classifier and TSI 3553 condensation particle counter). A 0.0457 cm impactor was used on the electrostatic classifier with a sample flow rate of 300 SCCM and a sheath flow rate of 3000 SCCM.

3. Instrument Performance

3.1 Detection limits

Allan deviation (Allan 1966) provides a measure of an instrument's long-term stability and has been widely used to provide the detection limits for instruments. We conducted an overlapping Allan deviation analysis (Figure 2a) by flowing dry nitrogen gas through the PAS cell for approximately 11 hours while recording the microphone signal. The microphone signal was normalized to the photodiode signal but was otherwise uncorrected for changes in the background (e.g., from drifts in the resonant frequency). The inflection point in the Allan deviation curve when plotted on a log-log scale represents the averaging time for which drift dominates over random noise as the primary source of error. The instrument was found to be stable to at least 1000 seconds for all channels, which indicates that drift will limit the ability to achieve the ultimate detection limit after this time unless the instrument is re-zeroed. In making ambient measurements, we re-zero every 30 minutes (1800 seconds), and thus drift does not significantly degrade the detection limits. The longer stability of the red and near-IR channels is likely due to the fact that those two channels are closer to the exact resonant frequency of the cell (± 1 Hz) than the blue and green channels (± 3 Hz) (See Figure S1, Supplemental Information) and are therefore likely less influenced by small changes in the resonant frequency and/or quality factor, *Q,* of the cell. The ultimate detection limits (2σ) observed from Allan deviation range from 0.1 Mm^{-1} at 662 nm to 0.2 Mm^{-1} at 406 nm.

[Figure 2]

Allan deviation provides a best-case scenario for the detection limit, and the standard deviation may provide a more accurate indicator of the practical detection limit. We therefore performed an alternate analysis on the nitrogen data in which they were corrected for baseline drift by averaging two-minute "background" blocks once every thirty minutes. The two background measurements from either side of each 28-minute "sample" period were averaged and subtracted from the sample period data, a method similar to that used by Nakayama et al. (Nakayama et al. 2015). The standard deviations then provide a measure of the instrument's practical detection limit, here limited by the two-minute average of the background data. The background-subtracted time series are shown in Figure 2b together with histograms of the data. Based on the standard deviation of that data, we calculate two-minute method detection limits (2σ) of 0.71, 0.62, 0.61, and 0.75 Mm^{-1} for the 406, 532, 662, and 785 nm PAS wavelengths, respectively, and 0.54 Mm^{-1} for the 662 nm CRD. These limits are sufficient to measure absorption and extinction of ambient aerosol under all but the cleanest of conditions (see Figure 3, for example).

[Figure 3]

The detection limits for the MultiPAS-IV compare favorably to those reported for other PAS instruments. For example, Nakayama et al. report 10-minute average, 2σ detection limits for the PASS-3 of 1.0 (405 nm), 1.9 (532 nm), and 0.7 Mm^{-1} (781 nm) (Nakayama et al. 2015), and Linke et al. recently reported 2σ limits of 3.7 (445 nm), 4.4 (532 nm), and 12 Mm^{-1} (660 nm) (Linke et al. 2016) for their 3-wavelength, single cell PAS, as well. The instruments of Lack and co-workers, upon which the MultiPAS-IV were based, exhibit much lower 2σ detection limits than it does: 0.16 Mm^{-1} (532 nm, 60 second average) (Lack et al. 2006) and 0.2 (404 nm), 0.15 (532 nm), and 0.4 Mm^{-1} (659 nm) for 1 second averages (Lack et al. 2012). Some of the higher sensitivity could be attributed to the higher multipass mirror reflectivity possible in those cells since they are designed for single wavelengths whereas the MultiPAS-IV uses a single set of mirrors for all four wavelengths thereby compromising some performance to achieve single-cell spectral coverage. A more extensive comparison of the detection limits of recent aerosol PAS instruments is given in Table S1 in the Supplemental Information.

3.2 Validation with nigrosin particles and a 7-wavelength aethalometer

To test the accuracy of the instrument, we measured the absorption of size-selected nigrosin particles. Nigrosin aerosol was generated using a constant output atomizer (TSI 3076) with an aqueous solution of nigrosin (Sigma Aldrich, CAS# 8005-03-6); particles were dried by passing them through two silica-gel diffusion driers in series. Nigrosin is a strongly absorbing substance comprised of organic dyes and is convenient for use here because it is water-soluble making it possible to aerosolize and forms spherical particles after drying (Lack et al. 2006). It has also been used by others to validate PAS (Lack et al. 2006; Wiegand et al. 2014; Radney and Zangmeister 2015), extinction-scattering (Dial et al. 2010), and photothermal interferometric (Sedlacek and Lee 2007) instruments. Furthermore, its complex refractive index has been measured recently over the range 300 – 800 nm (Bluvshtein et al. 2017) making it possible to calculate absorption cross sections using Mie theory. Thus, it is possible for us to compare absorption cross sections measured with the MultiPAS-IV to calculated values. To do so, we measured the absorption by particles that had been atomized, dried after passing through two diffusion driers (RH < 5%), and size selected using a differential mobility analyzer (DMA). We then calculated the absorption cross section as the ratio of the measured absorption and the particle number density as measured with a condensation particle counter (CPC).

In Figure 4 we show the measured and calculated absorption cross sections for four particle diameters, 500, 550, 600, and 650 nm. No corrections for doubly-charged particles transmitted by the DMA are necessary since an impactor with a nominal 50% cutpoint of 900 nm was used; additionally, very few particles that large are produced by the atomizer, the output of which was centered at approximately 100 nm. The error bars represent the precision of the CPC measurements added in quadrature to the precision of the PAS signal and the estimated PAS calibration uncertainty (7.6%). The Mie theory calculations were made using the refractive index values reported by (Bluvshtein et al. 2017) and by assuming that the geometric standard deviation of the particle sizes transmitted by the DMA was 1.05 (though the calculations are fairly insensitive to this value). The good agreement (2% root-mean-square-deviation) confirms the accuracy of the measurements made with the PAS, especially considering that uncertainties associated with the DMA and the refractive indices of nigrosin are not included. Additionally, it further validates the proposal put forth by Bluvshtein et al. to use nigrosin particles for PAS calibration (Bluvshtein et al. 2017); using all four wavelengths, we obtain a calibration constant with nigrosin that is within 5% of the one we obtained using NO_2 (see Figure S2 in the Supplemental Information). What is more, this nigrosin test confirms the validity of using the calibration obtained with NO_2 at 662 nm for other wavelengths and for particles.

[Figure 4]

As a further test of the instrument performance, we measured ambient aerosols in Athens, Georgia that had been dried to less than 10% relative humidity using both the MultiPAS-IV and a commercial 7-wavelength aethalometer (Figure 3). Over the three-day period, the instruments tracked each other well even though absorption was observed to range by approximately two orders of magnitude. This correlation is better demonstrated in Figure S3 (Supplemental

Information) in which the aethalometer absorption is plotted vs. MultiPAS-IV absorption at the nearest (or interpolated) wavelength with R^2 values ranging from 0.86 to 0.91. Such correlation demonstrates the ability of the MultiPAS-IV to make measurements of aerosol absorption under ambient conditions autonomously. Furthermore, this comparison shows that absorption by trace gas species, such as NO_2, did not contribute significantly to the PAS measurements since the aethalometer is not susceptible to such interference. Upon closer inspection of Figures 3 and S3, though, it is apparent that the aethalometer systematically overestimates the absorption. Given the good performance of the MultiPAS-IV with nigrosin, this discrepancy is most likely the result of well-known artifacts of filter-based instruments due to multiple scattering effects (see discussion in Section S.1 of the Supplemental Information).

3.3 Measuring the black carbon AAE of ambient aerosols

One of the goals in building the MultiPAS-IV instrument was to allow real-time measurement of aerosol absorption throughout the visible spectrum such that the value of the black carbon absorption Ångström exponent (AAE_{BC}) could be determined and used to derive the BrC contribution. By measuring the absorption at all four wavelengths in the same photoacoustic cell, many potential systematic errors associated with using separate PAS instruments that could affect the spectral shape can be minimized; for example, the cell calibration constant will be the same for all wavelengths and will not factor into calculations of the AAE. Here, we take two approaches to measuring AAE_{BC}: in the first, which we term the "two-wavelength approach," we calculate AAE_{BC} from the following equation using the absorption measured at a pair of wavelengths, λ_1 = 662 nm and λ_2 = 785 nm:

$$AAE_{BC} = \frac{ln\left(\frac{\alpha_{abs,\lambda_1}}{\alpha_{abs,\lambda_2}}\right)}{ln\left(\frac{\lambda_2}{\lambda_1}\right)} \qquad (3)$$

where $\alpha_{abs,\lambda}$ is the absorption at wavelength λ. This approach is equivalent to assuming that all absorption at these two wavelengths is attributed to BC alone.

In the second approach, the "three-wavelength approach," we use the absorption measured at 532 nm, 662 nm, and 785 nm and perform a non-linear least squares fit to the following equation to derive AAE_{BC}:

$$\alpha_{abs,\lambda} = \beta\lambda^{-AAE_{BC}} \qquad (4)$$

where β is a scaling factor. This approach has the benefit that it derives AAE_{BC} based on three wavelengths instead of two and over a wider spectral range, though it is equivalent to assuming that there is no BrC contribution at any of the three wavelengths. We note that this assumption may not be valid, especially at 532 nm. In both approaches, any data points that do not satisfy the condition $\alpha_{abs,406} > \alpha_{abs,532} > \alpha_{abs,662} > \alpha_{abs,785} > 0$ Mm^{-1} are discarded, which is equivalent to requiring the overall AAE to be greater than zero. This criterion results in 23% of the points being omitted, almost all of which were at low absorption (92% with $\alpha_{abs,785} < 2$ Mm^{-1}).

In the two-wavelength approach, we find that the median value of AAE_{BC} is 0.70 (± 0.38) with an interquartile range (IQR, 25th percentile to 75th percentile) of 0.41 - 1.10 (see Figure 5a). The error bars represent the uncertainty on the ratio of absorption at 662 nm and 785 nm propagated through equation 3; the largest source of error originates from the power meter used to calibrate the photodiode (5%) at each wavelength. The median AAE_{BC} value is low compared to the commonly assumed value of 1.0 (Bond and Bergstrom, 2006), but it is still within the range of possible values especially considering that the particles may be coated (Gyawali et al. 2009; Lack and Cappa 2010; D. Liu et al. 2015). What is more, (Wang et al. 2016) found that 60% of AAE values calculated from the 675 / 880 nm pair from the worldwide Aerosol Robotic Network (AERONET) were < 1. By way of comparison, the AAE_{BC} values calculated from the aethalometer measurements are 0.73 using the 880nm / 950 nm pair and 1.40 using the 660 nm / 880 nm pair (see Figure S4). The value of AAE_{BC} can also be seen in Figure 5a to vary quite a bit, which is probably more indicative of the high degree of sensitivity of AAE_{BC} to small changes in absorbance values than of true changes in the value of AAE_{BC}. For example, the absorbance at 662 nm relative to that at 785 nm only needs to change by 5% to cause the AAE_{BC} to increase from 0.70 to 1.0.

[Figure 5]

With the three-wavelength approach, the median AAE_{BC} is 1.18 (IQR = 1.03 - 1.33) (Figure 5b). We do not report an uncertainty on this value because propagation of uncertainty through the non-linear least squares power law fit to the three measured absorption values at each time point is not straightforward. However, the much smaller spread in values compared to the two-wavelength approach suggests that the inclusion of a third measurement (at 532 nm) improves the quality of the spectral fit, though it does so at the expense of assuming that all absorption at 532 nm is attributed to BC. Such an assumption is probably not warranted since numerous studies have found that BrC can also absorb at this wavelength; for example, offline measurements of solvent-extracted (i.e. not BC) particulate matter demonstrate absorption to at least 600 nm (Kirchstetter et al. 2004; Hecobian et al. 2010; Zhang et al. 2013; Phillips and Smith 2017a). Likewise, some laboratory-generated BrC have been found to absorb at 532 nm and beyond (e.g. (Shapiro et al. 2009);(Romonosky et al. 2016)). For this reason, the AAE_{BC} values derived with this approach probably represent an upper limit, and the true value of AAE_{BC} probably lies somewhere between 0.70 and 1.18 as measured with the two approaches.

While a smaller degree of scatter would be desirable, we point out that this is the first PAS instrument to measure AAE_{BC} at low ambient absorbance values. To put this into context, 36% of the samples had a 785 nm absorbance of less than 2 Mm^{-1}, which is equivalent to a BC loading of less than 0.4 $\mu g/m^3$ (assuming a mass absorption cross section of 5.25 m^2/g). With such small absorbance and the high degree of sensitivity of AAE_{BC} to the relative absorption at 662 nm and 785 nm, it is not surprising that such a spread is observed. Interestingly, the median calculated AAE_{BC} values and variances are independent of the magnitude of 785 nm absorption when it is greater than 2 Mm^{-1} (Figure S5), indicating that our ability to measure AAE_{BC} is not limited by the magnitude of absorption above this value.

3.4 Measuring brown carbon absorption of ambient aerosols

At UV and near-UV wavelengths, aerosol absorption likely comprises contributions from both BC and BrC components. The ability to measure AAE_{BC} in real time with the two-wavelength approach allows us to also estimate the BrC contribution at 406 nm and 532 nm:

$$\alpha_{BrC,\lambda} = \alpha_{abs,\lambda} - \alpha_{BC,\lambda} = \alpha_{abs,\lambda} - \alpha_{abs,785}\left(\frac{\lambda}{785\ nm}\right)^{-AAE_{BC}} \quad (5)$$

where $\alpha_{BrC,\lambda}$ is the calculated absorption attributed to BrC at wavelength λ (406 nm or 532 nm). With this approach, we do not assume a value of AAE_{BC} to extrapolate the BC contribution to 406 nm and 532 nm from longer wavelengths. Instead, we use the value of AAE_{BC} measured with the PAS at each time point (from equation 3), which gives us a direct measure of the wavelength dependence of the BC aerosol absorption. This approach would not be possible without having the two wavelengths (red and near-IR) that can be attributed solely to BC, and as such this instrument is the only aerosol PAS that we are aware of that can measure AAE_{BC} of suspended aerosols. Importantly, then, this value includes any effects of coatings or morphology (Lack and Cappa 2010), which could confound the attribution of BrC absorption if not accounted for correctly, as Lack and Langridge have demonstrated (Lack and Langridge 2013). Using this value, we can derive a more representative estimate of the BrC absorption at shorter wavelengths. We point out that this approach assumes that the AAE_{BC} is independent of wavelength, a commonly-made assumption (Bond and Bergstrom 2006).

Figure 6a shows the derived BrC absorption time series at both 406 nm and 532 nm calculated using Equation 5. The BrC absorption is seen to vary greatly, but it generally correlates with the overall absorption time series (Figure 3). The percentage absorption due to BrC at both wavelengths is shown in Figure 6b, and despite the considerable variability they remain fairly constant about the median values of 43% (IQR = 30% - 52%) for 406 nm and 13% (IQR = 3% - 21%) for 532 nm. The scatter observed is a function of both the small absorbance being measured and the scatter in the calculated AAE_{BC} values (Figure 5a) used to calculate the BrC absorption. However, the calculated BrC percentages are more or less the same across the range of absorbance measured, especially when $\alpha_{abs,785} > 2$ Mm^{-1} (see Figure S5). It is apparent that there is no significant trend in the BrC percentages with time suggesting that the relative contributions of BrC and BC in the aerosols did not change much over the study.

[Figure 6]

It is also possible to derive BrC absorption using the AAE_{BC} calculated with the three-wavelength (532 nm / 662 nm / 785 nm) approach (Figure S6). In this case, Equation 5 is modified slightly to extrapolate the BC component from the average of the absorption measured at 662 nm and 785 nm:

$$\alpha_{BrC,\lambda} = \alpha_{abs,\lambda} - \frac{(\alpha_{abs,662} + \alpha_{abs,785})}{2}\left(\frac{\lambda}{723.5\ nm}\right)^{-AAE_{BC}} \quad (6)$$

taking advantage of having two wavelengths at which the absorption is dominated by BC. The larger AAE_{BC} values (median = 1.18, IQR = 1.03 – 1.33) with this approach result in smaller BrC absorption with a median BrC absorption at 406 nm of 26% (IQR = 20% - 31%). Of course, since the 532 nm absorption is assumed to originate solely from the BC with this approach, there is on average no BrC absorption at this wavelength. Alternatively, we can assume $AAE_{BC} = 1.0$, as is commonly done when no concurrent measurements of the BC wavelength dependence are available, and use Equation 6 to derive the BrC contributions at 406 nm (33%, IQR = 27% -

36%) and 532 nm (6%, IQR = 2% - 10%) (Figure S7).

3.5 Measuring the AAE of brown carbon in ambient aerosols

The ability to calculate the BrC contribution to aerosol absorption at both 406 nm and 532 nm using the two-wavelength approach to calculate the AAE_{BC} also makes it possible to calculate the AAE_{BrC} using Equation 3 (with AAE_{BC} replaced by AAE_{BrC}). We point out that this capability is unique to this PAS with its four wavelengths, two in the red/near-IR for determining AAE_{BC} and two in the blue/green for determining AAE_{BrC}. The time series of the AAE_{BrC} is shown in Figure 6c in which only the time points for which BrC absorption is greater than 0 Mm^{-1} for both 406 nm and 532 nm have been used; this includes 79% of the time points. The median AAE_{BrC} is 6.3 (± 0.9) (IQR = 5.1 - 7.4) with no apparent trend with time over the course of the study. Here, the uncertainty on AAE_{BrC} is propagated from the uncertainty on AAE_{BC} (used to derive the BrC contribution), for which the largest source of error originates from the power meter used to calibrate the photodiode. The corresponding uncertainty on AAE_{BC} is ± 0.38, though interestingly, its impact on AAE_{BrC} is mitigated by the fact that it propagates in the same direction for both the 406 nm and 532 nm BrC calculations; thus, the uncertainty partially cancels.

The AAE_{BrC} values measured in this study are similar to AAEs we measured for water- (6.1 ± 0.7) and methanol-soluble (6.7 ± 1.1) filter-collected samples in Athens, Georgia (Phillips and Smith 2017b) as well as values reported by others. For example, Weber and co-workers report AAEs of 6 - 8 and 4 – 6 for water- and methanol soluble particulate matter, respectively, collected in Atlanta, Georgia (Hecobian et al. 2010; J. Liu et al. 2013), 6.82 ± 2.63 (water-soluble) and 4.54 ± 3.07 (methanol-soluble) in the Central U.S. (J. Liu et al. 2015), and 7.28 ± 0.24 (water-soluble) and 7.10 ± 0.45 (methanol-soluble) in Beijing, China (Cheng et al. 2016). Likewise, Hoffer et al. measured average water-soluble AAEs of 6.4 and 6.8 for daytime and nighttime samples in Brazil, respectively (Hoffer et al. 2006), and Kim et al. measured average AAEs of 7.23 ± 1.58 (water-soluble) and 5.05 ± 0.67 (methanol-soluble) in Seoul, Korea (Kim et al. 2016).

As with the AAE_{BC} values and the 406 nm and 532 nm BrC absorption values, there appears to be no correlation between the AAE_{BrC} and the magnitude of absorption at 785 nm (see Figure S5). This observation suggests that the spectral shape of the BrC was not a function of aerosol loading. Furthermore, the spread of AAE_{BrC} values was relatively independent of absorption demonstrating no improvement for $\alpha_{abs,785}$ values above 2 Mm^{-1}, which indicates that the ability to derive the AAE_{BrC} values is not limited by the instrument's sensitivity except perhaps at the lowest absorbance values.

4.0 Conclusions and Outlook

We have created a 4-wavelength photoacoustic spectrometer capable of measuring ambient aerosol absorption, which to the best of our knowledge is the first such multi-wavelength, multipass, single-cell PAS. The instrument is compact, robust, and portable, such that it may easily be deployed in field and laboratory campaigns and demonstrates good correlation with a 7-wavelength aethalometer. The instrument makes several improvements upon existing instrumentation, including:

1. making possible the calculation of both AAE_{BC} and AAE_{BrC} directly from the absorption measurements,

2. employing a single cell for all wavelengths thereby removing cell-to-cell calibration uncertainties and improving the accuracy of AAE calculations,

3. and achieving sub-Mm^{-1} detection limits for four wavelengths spanning the UV-visible spectrum in a portable instrument free from filter artifacts.

We believe this instrument will allow more accurate measurement of the AAE and thereby reduce uncertainty on aerosol absorption and further allow better differentiation between BC and BrC. Future efforts will focus on expanding spectral coverage into the UV to improve this differentiation even more.

Acknowledgements

The authors gratefully acknowledge support for this work by the National Science Foundation (AGS-1241621 and AGS-1638307). They also wish to thank Prof. Rawad Saleh (School of Engineering, University of Georgia) for loan of the aethalometer, atomizer, and a diffusion drier used in this study and the UGA Instrument Shop for construction of the PAS and CRD cells.

References

Ajtai, T., Filep, A., Schnaiter, M., Linke, C., Vragel, M., Bozoki, Z., Szabo, G., and Leisner, T. (2010). A novel multi-wavelength photoacoustic spectrometer for the measurement of the UV-vis-NIR spectral absorption coefficient of atmospheric aerosols. *J. Aerosol Sci,* 41(11):1020–1029.

Ajtai, T., Filep, A., Utry, N., Schnaiter, M., Linke, C., Bozoki, Z., Szabo, G., and Leisner, T. (2011). Inter-comparison of optical absorption coefficients of atmospheric aerosols determined by a multi-wavelength photoacoustic spectrometer and an Aethalometer under sub-urban wintry conditions. *J. Aerosol Sci,* 42(12):859–866.

Allan, D.W. (1966). Statistics of atomic frequency standards. *Proc. IEEE,* 54(2):221–230.

Andreae, M.O. and Gelencser, A. (2006). Black carbon or brown carbon? The nature of light-absorbing carbonaceous aerosols. *Atmos. Chem. Phys,* 6(10):3131–3148.

Arnott, W.P., Rogers, C., Jin, T., and Bruch, R. (1999). Photoacoustic spectrometer for measuring light absorption by aerosol: Instrument description. *Atmos. Environ,* 33(17):2845–2852.

Arnott, W.P., Walker, J.W., Moosmüller, H., Elleman, R.A., Jonsson, H.H., Buzorius, G., Conant, W.C., Flagan, R.C., and Seinfeld, J.H. (2006). Photoacoustic insight for aerosol light absorption aloft from meteorological aircraft and comparison with particle soot absorption photometer measurements: DOE Southern Great Plains climate research facility and the coastal stratocumulus imposed perturbation experiments. *J. Geophys. Res,* 111(D5):605.

Bell, A.G. (1881). The production of sound by radiant energy. *Science,* 2(49):242–253.

Berden, G. and Engeln, R. (Eds.) (2009). Cavity Ring-Down Spectroscopy*, Cavity Ring-Down Spectroscopy*. John Wiley & Sons, Ltd, Chichester, UK.

Bluvshtein, N., Flores, J.M., He, Q., Segre, E., Segev, L., Hong, N., Donohue, A., Hilfiker, J.N., and Rudich, Y. (2017). Calibration of a multi-pass photoacoustic spectrometer cell using light-absorbing aerosols. *Atmos. Meas. Tech,* 10(3):1203–1213.

Bond, T.C. and Bergstrom, R.W. (2006). Light absorption by carbonaceous particles: An investigative review. *Aerosol Sci. Technol,* 40(1):27–67.

Bond, T.C., Doherty, S.J., Fahey, D.W., Forster, P.M., Berntsen, T., DeAngelo, B.J., Flanner, M.G., Ghan, S., Kaercher, B., Koch, D., Kinne, S., Kondo, Y., Quinn, P.K., Sarofim, M.C., Schultz, M.G., Schulz, M., Venkataraman, C., Zhang, H., Zhang, S., Bellouin, N., Guttikunda, S.K., Hopke, P.K., Jacobson, M.Z., Kaiser, J.W., Klimont, Z., Lohmann, U., Schwarz, J.P., Shindell, D., Storelvmo, T., Warren, S.G., and Zender, C.S. (2013). Bounding the role of black carbon in the climate system: A scientific assessment. *J. Geophys. Res.: Atmos,* 118(11):5380–5552.

Bostrom, G., Atkinson, D., and Rice, A. (2015). The discrete Fourier transform algorithm for determining decay constants—Implementation using a field programmable gate array. *Rev. Sci. Instrum,* 86(4):043106.

Brown, S.S. (2003). Absorption spectroscopy in high-finesse cavities for atmospheric studies. *Chem. Rev,* 103(12):5219–5238.

Cheng, Y., He, K.-B., Du, Z.-Y., Engling, G., Liu, J.-M., Ma, Y.-L., Zheng, M., and Weber, R.J. (2016). The characteristics of brown carbon aerosol during winter in Beijing. *Atmos. Environ,* 127:355–364.

Dial, K.D., Hiemstra, S., and Thompson, J.E. (2010). Simultaneous Measurement of Optical Scattering and Extinction on Dispersed Aerosol Samples. *Anal. Chem,* 82(19):7885–7896.

Drinovec, L., Močnik, G., Zotter, P., Prevot, A.S.H., Ruckstuhl, C., Coz, E., Rupakheti, M., Sciare, J., Mueller, T., Wiedensohler, A., and Hansen, A.D.A. (2015). The “dual-spot” Aethalometer: an improved measurement of aerosol black carbon with real-time loading compensation. *Atmos. Meas. Tech,* 8(5):1965–1979.

Everest, M.A. and Atkinson, D.B. (2008). Discrete sums for the rapid determination of exponential decay constants. *Rev. Sci. Instrum,* 79(2):023108.

Gyawali, M., Arnott, W.P., and Lewis, K.A. (2009). In situ aerosol optics in Reno, NV, USA during and after the summer 2008 California wildfires and the influence of absorbing and non-absorbing organic coatings on spectral light absorption. *Atmos. Chem. Phys,* 9(20):8007–8015.

Haisch, C., Menzenbach, P., Bladt, H., and Niessner, R. (2012). A Wide Spectral Range Photoacoustic Aerosol Absorption Spectrometer. *Anal. Chem,* 84:8941–8945.

Hecobian, A., Zhang, X., Zheng, M., Frank, N., Edgerton, E.S., and Weber, R.J. (2010). Water-soluble organic aerosol material and the light-absorption characteristics of aqueous extracts measured over the Southeastern United States. *Atmos. Chem. Phys,* 10(13):5965–5977.

Hoffer, A., Gelencser, A., Guyon, P., and Kiss, G. (2006). Optical properties of humic-like substances (HULIS) in biomass-burning aerosols. *Atmos. Chem. Phys,* 6(11):3563–3570.

Kim, H., Kim, J.Y., Jin, H.C., Lee, J.Y., and Lee, S.P. (2016). Seasonal variations in the light-absorbing properties of water-soluble and insoluble organic aerosols in Seoul, Korea. *Atmos. Environ,* 129:234–242.

Kirchstetter, T.W., Novakov, T., and Hobbs, P. (2004). Evidence that the spectral dependence of light absorption by aerosols is affected by organic carbon. *J. Geophys. Res,* 109:D21208–doi:10.1029–2004JD004999.

Lack, D.A. and Cappa, C.D. (2010). Impact of brown and clear carbon on light absorption enhancement, single scatter albedo and absorption wavelength dependence of black carbon. *Atmos. Chem. Phys,* 10(9):4207–4220.

Lack, D.A. and Langridge, J.M. (2013). On the attribution of black and brown carbon light absorption using the Ångström exponent. *Atmos. Chem. Phys,* 13:10535–10543.

Lack, D.A., Cappa, C.D., Covert, D.S., Baynard, T., Massoli, P., Sierau, B., Bates, T.S., Quinn, P.K., Lovejoy, E.R., and Ravishankara, A.R. (2008). Bias in filter-based aerosol light absorption measurements due to organic aerosol loading: Evidence from ambient measurements. *Aerosol Sci. Technol,* 42(12):1033–1041.

Lack, D.A., Lovejoy, E.R., Baynard, T., Pettersson, A., and Ravishankara, A.R. (2006). Aerosol absorption measurement using photoacoustic spectroscopy: Sensitivity, calibration, and uncertainty developments. *Aerosol Sci. Technol,* 40(9):697–708.

Lack, D.A., Richardson, M., Law, D., Langridge, J., Cappa, C.D., McLaughlin, R., and Murphy, D. (2012). Aircraft Instrument for Comprehensive Characterization of Aerosol Optical Properties, Part 2: Black and Brown Carbon Absorption and Absorption Enhancement Measured with Photo Acoustic Spectroscopy. *Aerosol Sci. Technol,* 46:555–568.

Lewis, K.A., Arnott, W.P., and Wold, C.E. (2008). Strong spectral variation of biomass smoke light absorption and single scattering albedo observed with a novel dual-wavelength photoacoustic instrument. *J. Geophys. Res.: Atmos,* 113(D16):D16203–doi: 10.1029–2007jd009699.

Lin, H.B. and Campillo, A.J. (1985). Photothermal aerosol absorption-spectroscopy. *Appl Opt,* 24(3):422–433.

Linke, C., Ibrahim, I., Schleicher, N., Hitzenberger, R., Andreae, M.O., Leisner, T., and Schnaiter, M. (2016). A novel single-cavity three-wavelength photoacoustic spectrometer for atmospheric aerosol research. *Atmos. Meas. Tech,* 9(11):5331–5346.

Liu, D., Taylor, J.W., Young, D.E., Flynn, M.J., Coe, H., and Allan, J.D. (2015). The effect of complex black carbon microphysics on the determination of the optical properties of brown carbon. *Geophys. Res. Lett,* 42(2):613–619.

Liu, J., Bergin, M.H., Guo, H., King, L., Kotra, N., Edgerton, E.S., and Weber, R.J. (2013). Size-resolved measurements of brown carbon in water and methanol extracts and estimates of their contribution to ambient fine-particle light absorption. *Atmos. Chem. Phys,* 13:12389–12404.

Liu, J., Scheuer, E., Dibb, J., Diskin, G.S., Ziemba, L.D., Thornhill, K.L., Anderson, B.E., Wisthaler, A., Mikoviny, T., Devi, J.J., Bergin, M.H., Perring, A.E., Markovic, M.Z., Schwarz, J.P., Campuzano-Jost, P., Day, D.A., Jimenez, J.L., and Weber, R.J. (2015). Brown carbon aerosol in the North American continental troposphere: sources, abundance, and radiative forcing. *Atmos. Chem. Phys,* 15(14):7841–7858.

Mazurenka, M., Wada, R., Shillings, A.J.L., Butler, T.J.A., Beames, J.M., and Orr-Ewing, A.J. (2005). Fast Fourier transform analysis in cavity ring-down spectroscopy: application to an optical detector for atmospheric NO_2. *Appl. Phys. B: Lasers Opt,* 81(1):135–141.

Miklos, A., Hess, P., and Bozoki, Z. (2001). Application of acoustic resonators in photoacoustic trace gas analysis and metrology. *Rev. Sci. Instrum,* 72(4):1937–1955.

Moosmüller, H., Arnott, W.P., and Rogers, C.F. (1997). Methods for real-time, in situ measurement of aerosol light absorption. *J. Air Waste Manage. Assoc,* 47(2):157–166.

Moosmüller, H., Chakrabarty, R.K., and Arnott, W.P. (2009). Aerosol light absorption and its measurement: A review. *J. Quant. Spectrosc. Radiat. Transfer,* 110(11):844–878.

Nakayama, T., Suzuki, H., Kagamitani, S., Ikeda, Y., Uchiyama, A., Matsumi, Y., matsumi (2015). Characterization of a three wavelength photoacoustic soot spectrometer (PASS-3) and a photoacoustic extinctiometer (PAX). *J. Meteorol. Soc. Jpn,* 93(2):285–308.

Onasch, T.B., Massoli, P., Kebabian, P.L., Hills, F.B., Bacon, F.W., and Freedman, A. (2015). Single scattering albedo monitor for airborne particulates. *Aerosol Sci. Technol,* 49(4):267–279.

Petzold, A. and Niessner, R. (1995). Novel design of a resonant photoacoustic spectrophone for

elemental carbon mass monitoring. *00036951,* 66(10):1285–1287.
Petzold, A. and Schönlinner, M. (2004). Multi-angle absorption photometry - a new method for the measurement of aerosol light absorption and atmospheric black carbon. *J. Aerosol Sci,* 35(4):421–441.
Phillips, S.M. and Smith, G.D. (2017a). Spectroscopic comparison of water-and methanol-soluble brown carbon particulate matter. *Aerosol Sci. Technol,* DOI: 10.1080–02786826.2017.1334109.
Phillips, S.M. and Smith, G.D. (2017b). Spectroscopic comparison of water-and methanol-soluble brown carbon particulate matter. *Aerosol Sci. Technol,* 1–9.
Radney, J.G. and Zangmeister, C.D. (2015). Measurement of Gas and Aerosol Phase Absorption Spectra across the Visible and Near-IR Using Supercontinuum Photoacoustic Spectroscopy. *Anal. Chem,* 87(14):7356–7363.
Romonosky, D.E., Ali, N.N., Saiduddin, M.N., Wu, M., Lee, H.J.J., Aiona, P.K., and Nizkorodov, S.A. (2016). Effective absorption cross sections and photolysis rates of anthropogenic and biogenic secondary organic aerosols. *Atmos. Environ,* 130:172–179.
Sedlacek, A. and Lee, J. (2007). Photothermal interferometric aerosol absorption spectrometry. *Aerosol Sci. Technol,* 41(12):1089–1101.
Shapiro, E., Szprengiel, J., Sareen, N., Jen, C., Giordano, M., and McNeill, V. (2009). Light-absorbing secondary organic material formed by glyoxal in aqueous aerosol mimics. *Atmos. Chem. Phys,* 9(7):2289–2300.
Sharma, N., Arnold, I.J., Arnott, W.P., and Mazzoleni, C. (2013). Photoacoustic and nephelometric spectroscopy of aerosol optical properties with a supercontinuum light source. 6(4):6293–6327.
Silver, J.A. (2005). Simple dense-pattern optical multipass cells. *Appl Opt,* 44(31):6545–6556.
Singh, S., Fiddler, M.N., Smith, D., and Bililign, S. (2014). Error analysis and uncertainty in the determination of aerosol optical properties using cavity ring-down spectroscopy, integrating nephelometry, and the extinction-scattering method. *Aerosol Sci. Technol,* 48(12):1345–1359.
Stocker, T.F., Qin, D., Plattner, G.K., Tignor, M., Allen, S.K., Boschung, J., Nauels, A., Xia, Y., Bex, V., and Midgley, P.M. (Eds.) (2014). Climate change 2013: The physical science basis: Working Group I contribution to the Fifth assessment report of the Intergovernmental Panel on Climate Change. Cambridge University Press, Cambridge, UK and New York, NY, USA.
Truex, T.J. and Anderson, J.E. (1979). Mass monitoring of carbonaceous aerosols with a spectrophone. *Atmos. Environ., Part A,* 13:507–509.
Wang, X., Heald, C.L., Sedlacek, A.J., de Sá, S.S., Martin, S., Alexander, M.L., Watson, T.B., Aiken, A.C., Springston, S.R., and Artaxo, P. (2016). Deriving brown carbon from multiwavelength absorption measurements: method and application to AERONET and Aethalometer observations. *Atmos. Chem. Phys,* 16:12733–12752.
Weingartner, E., Saathoff, H., Schnaiter, M., Streit, N., Bitnar, B., and Baltensperger, U. (2003). Absorption of light by soot particles: determination of the absorption coefficient by means of aethalometers. *J. Aerosol Sci,* 34:1445–1463.
Wiegand, J.R., Mathews, L.D., and Smith, G.D. (2014). A UV-Vis photoacoustic spectrophotometer. *Anal. Chem,* 86(12):6049–6056.
Zhang, X., Kim, H., Parworth, C.L., Young, D.E., Zhang, Q., Metcalf, A.R., and Cappa, C.D. (2016). Optical properties of wintertime aerosols from residential wood burning in Fresno, CA: Results from DISCOVER-AQ 2013. *Environ. Sci. Technol,* 50(4):1681–1690.
Zhang, X., Lin, Y.-H., Surratt, J.D., and Weber, R.J. (2013). Sources, composition and absorption Ångström exponent of light-absorbing organic components in aerosol extracts

from the Los Angeles Basin. *Environ. Sci. Technol,* 47(8):3685–3693.

Figures

Figure 1. Schematic diagram of the PAS. M = mirror, D = dichroic mirror, L = lens, BS = 90:10 beamsplitter, (A)PD = (avalanche) photodiode.

Figure 2. (a) Allan deviation plot of absorption (PAS, solid lines) and extinction (CRD, open circles) data collected with nitrogen gas, (b) time series and histograms of same data with re-zeroing every 30 minutes to simulate standard operation of the instruments (30 second average: dark grey lines, 2 minute average: light grey (colored) lines, 10 minute average: black lines). Dotted lines indicate ± 2 standard deviations of the 2-minute average data.

Figure 3. Time series of (a) absorption and extinction from the MultiPAS-IV, (b) absorption from the 7-wavelength aethalometer, and (c) size distribution data from the SMPS (grey (color) scale represents particle number density). The PAS/CRD curves represent 10-minute rolling averages of 1-second data; each aethalometer curve represents a 10-minute rolling average of 1-minute data.

Figure 4. Nigrosin aerosol absorption cross sections measured with the MultiPAS-IV for four different selected mobility diameters (500 nm: diamonds (green), 550 nm: triangles (brown), 660 nm: circles (red), 650 nm: squares (blue)). Curves are Mie theory calculations using the refractive index data of *(Bluvshtein et al. 2017)*.

Figure 5. Time series and histogram of AAE_{BC} values calculated using the absorbance values at: (a) 662 nm and 785 nm or (b) 532 nm, 662 nm, and 785 nm. Points are sized in relation to the magnitude of absorption at 785 nm. The median values of AAE_{BC} (0.70 and 1.18, respectively) are represented by the dark grey (blue) lines, and the interquartile ranges are represented by the light grey (light blue) shaded regions.

Figure 6. BrC as calculated using the two-wavelength approach to calculating AAE_{BC}. (a): Time series of calculated BrC absorption at 406 nm (dark grey (purple) open circles) and 532 nm light grey (green) open circles; (b): time series and histograms of fraction of absorption due to BrC at 406 nm (dark grey (purple) closed circles) and 532 nm (light grey (green) closed circles); (c): time series and histogram of BrC AAE ((orange) circles). Horizontal lines represent median values while shaded regions represent interquartile ranges.

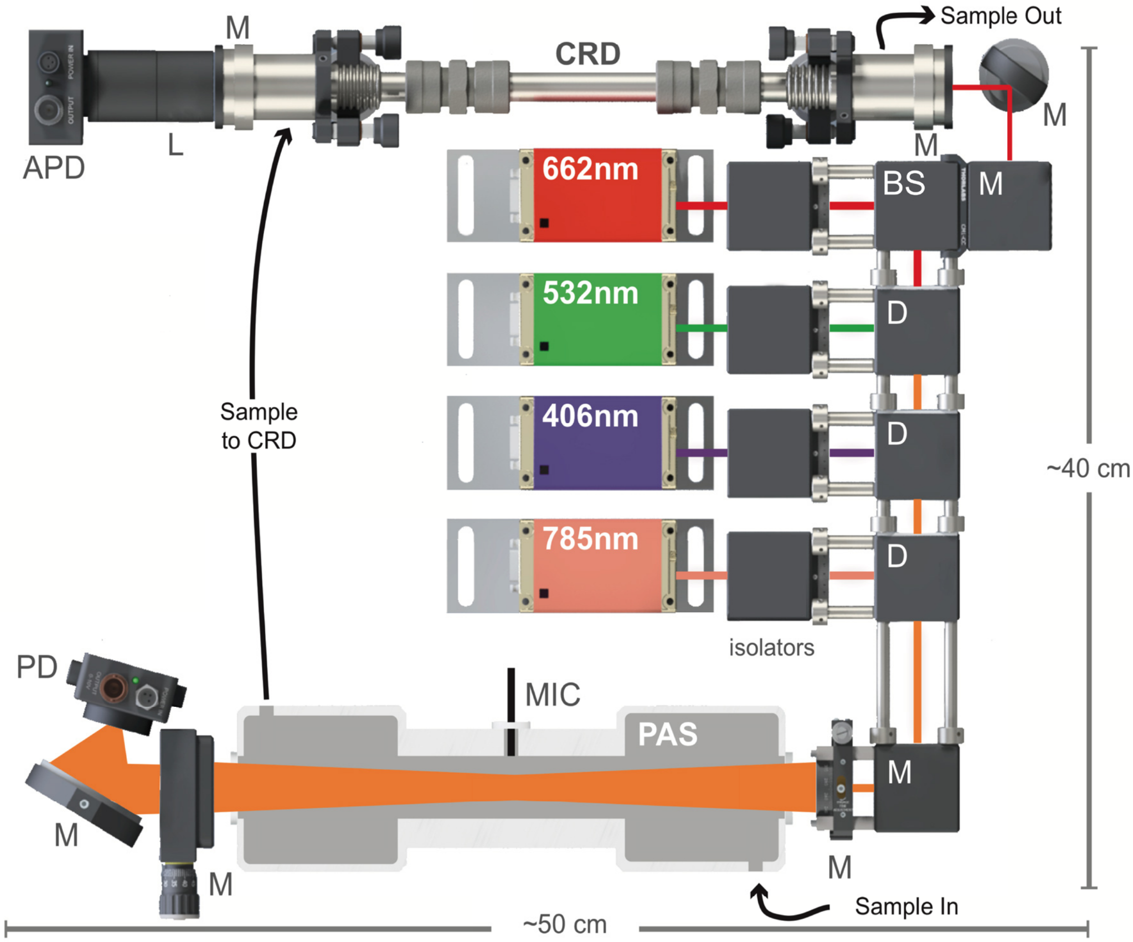

APD
L
M
CRD
Sample Out
M
M
BS
M
662nm
532nm
406nm
785nm
D
D
D
isolators
Sample
to CRD
~40 cm
PD
MIC
PAS
M
M
M
M
Sample In
~50 cm

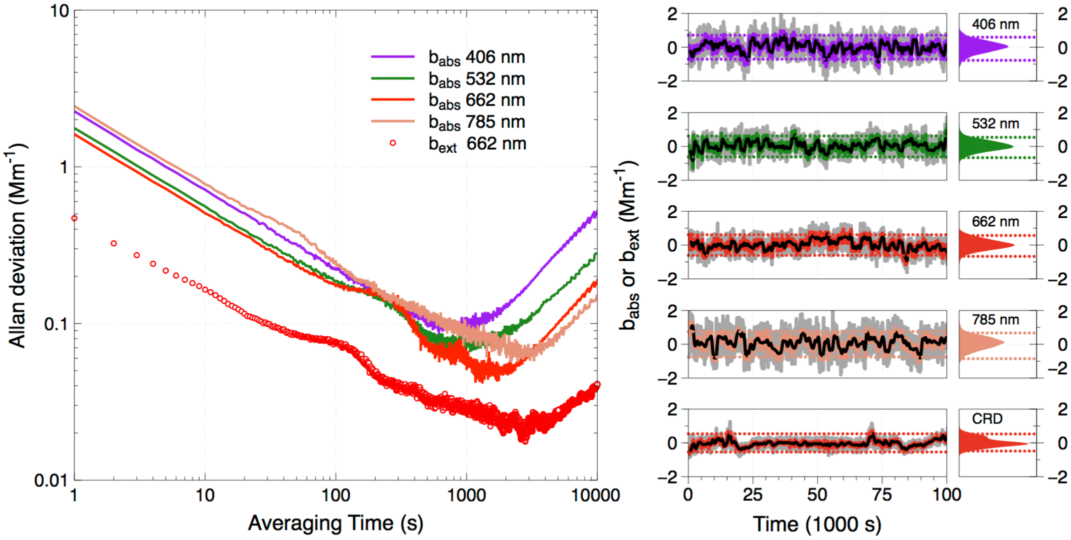

Allan deviation (Mm^{-1})
Averaging Time (s)
b_{abs} 406 nm
b_{abs} 532 nm
b_{abs} 662 nm
b_{abs} 785 nm
b_{ext} 662 nm
b_{abs} or b_{ext} (Mm^{-1})
Time (1000 s)
406 nm
532 nm
662 nm
785 nm
CRD

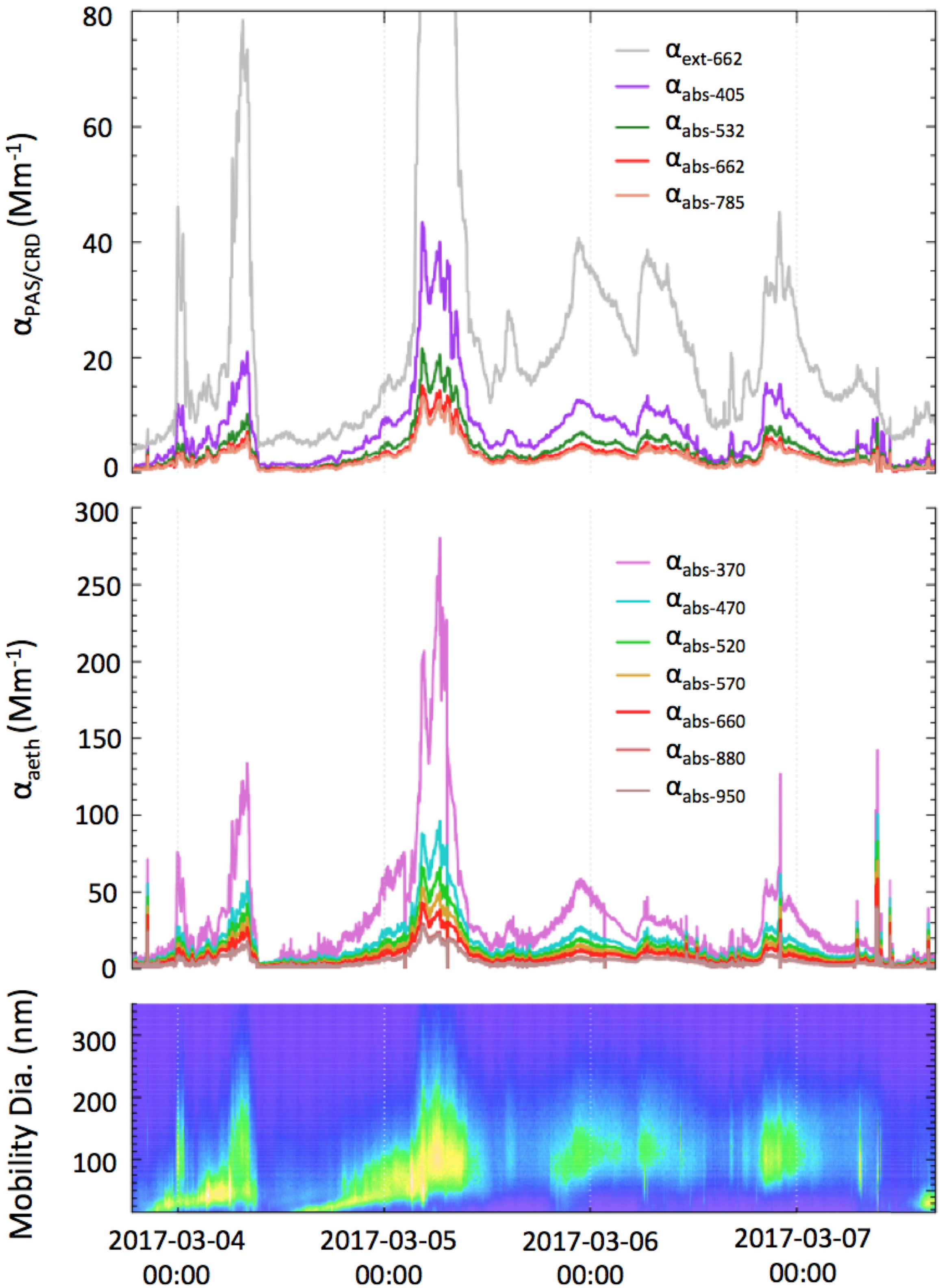

80
60
40
20
0
$\alpha_{PAS/CRD}$ (Mm^{-1})
$\alpha_{ext-662}$
$\alpha_{abs-405}$
$\alpha_{abs-532}$
$\alpha_{abs-662}$
$\alpha_{abs-785}$
300
250
200
150
100
50
0
α_{aeth} (Mm^{-1})
$\alpha_{abs-370}$
$\alpha_{abs-470}$
$\alpha_{abs-520}$
$\alpha_{abs-570}$
$\alpha_{abs-660}$
$\alpha_{abs-880}$
$\alpha_{abs-950}$
300
200
100
Mobility Dia. (nm)
2017-03-04 00:00
2017-03-05 00:00
2017-03-06 00:00
2017-03-07 00:00

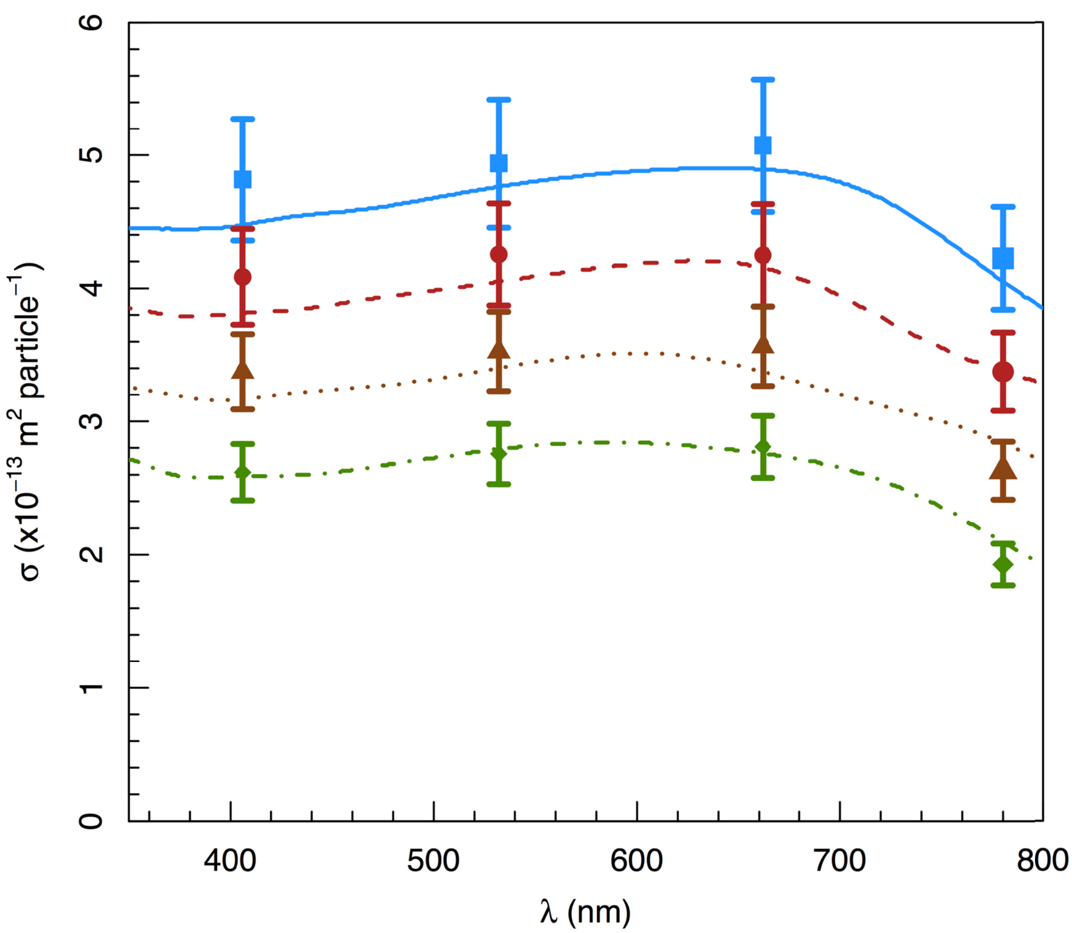

σ (x10^-13 m^2 particle^-1)
0
1
2
3
4
5
6
400
500
600
700
800
λ (nm)

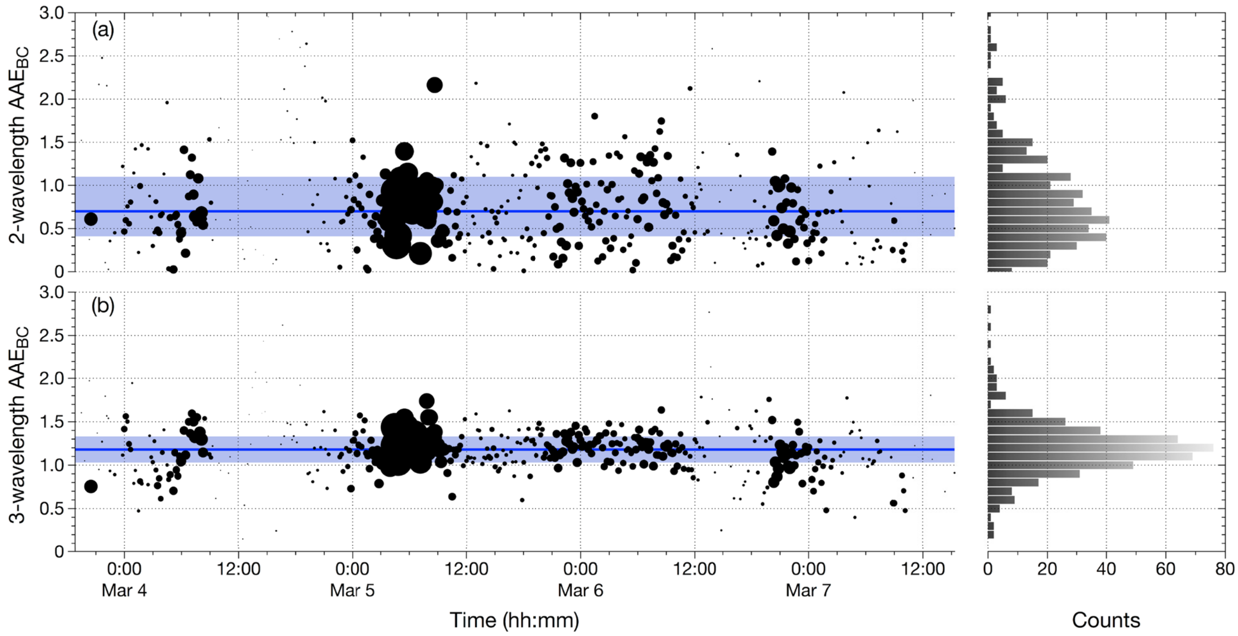

(a)
(b)
2-wavelength AAE_{BC}
3-wavelength AAE_{BC}
0:00
Mar 4
12:00
0:00
Mar 5
12:00
0:00
Mar 6
12:00
0:00
Mar 7
12:00
Time (hh:mm)
0
20
40
60
80
Counts

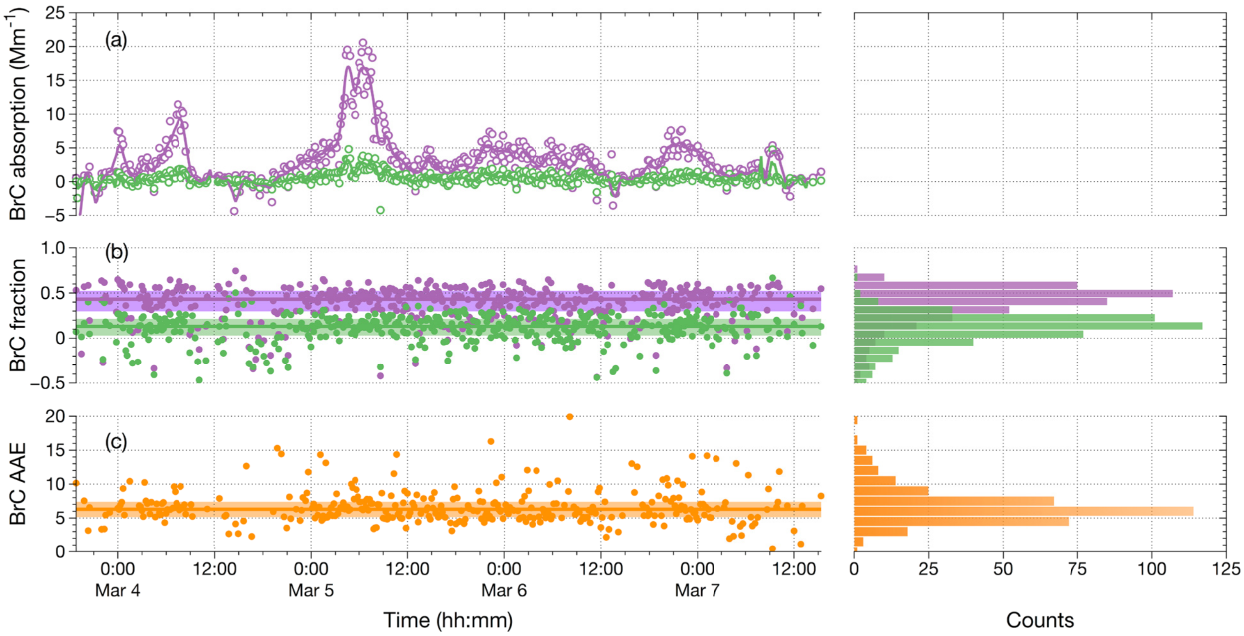

BrC absorption (Mm^{-1})
(a)
(b)
BrC fraction
(c)
BrC AAE
0:00
Mar 4
12:00
0:00
Mar 5
12:00
0:00
Mar 6
12:00
0:00
Mar 7
12:00
Time (hh:mm)
Counts